where *H(A)* is the entropy of the first image (i.e., the portal image), *H(B)* is the entropy of the second image (i.e., the DRR image), and *H(A,B)* is the entropy of their joined histogram.[7]

Optimizing the MI involves finding the x-y shift position that yields the highest mutual information coefficient, automatically shifting the portal image left, right, up and down a determined step size, and choosing the position with the highest MI coefficient. If the current x-y shift value yields the highest MI coefficient, the optimization loop is abandoned. In order to reduce the likelihood of stopping at a local maximum, we employ a multiresolution method. The initial step size is relatively large, usually 4 mm. The best MI coefficient is located with the initial step size. The step size is then reduced by half and the process is repeated. The final step size is usually 1 mm, but can be set lower for submillimeter accuracy.

Adding rotation checks can increase optimization time exponentially if every possible rotation is checked at each shift location. However, if we assume that the setup rotation is small, a good compromise approach is to search rotation and shift iteratively; that is, search for the best x-y shift and then search for the best rotation. This process is repeated until the best possible rotation is found at the best possible x-y shift.

## D. Phantom study

CT scans of anthropomorphic thorax and pelvis phantoms were taken. The images were read into a commercial treatment planning software system (Xio; CMS, Inc., St. Louis, MO). DRR images (one for the thorax, one for the pelvis) were generated using an antero-posterior (AP) port with a 10 × 10 cm square field.

In order to be able to present a portal image with a known but arbitrary x-y error offset, we first obtained a single portal image of the phantom without field or scale ticks. Our test software burns in the treatment field and tick marks based on determined horizontal and vertical offset error values (Fig. 4). The portal images of the phantoms were acquired with a 6 MV photon beam from a linear accelerator. A list of five cases was prepared with offset values between plus and minus 10 mm horizontally and vertically. Rotation was not considered in this study. In order to determine each subject's consistency in determining the offset error, each case was presented twice for a total of ten cases. Each subject was presented with the same offset cases, but the order of the case list was shuffled.

For the ten thorax and ten pelvis cases generated by the computer with the above method, we presented the series of cases to each examiner using three methods. First, five licensed radiation oncologists determined setup error with the conventional side-by-side method, without the aid of the registration software. We refer to this as the "side-by-side method". These doctors included experienced physicians, as well as doctors in training. Four radiation technicians were

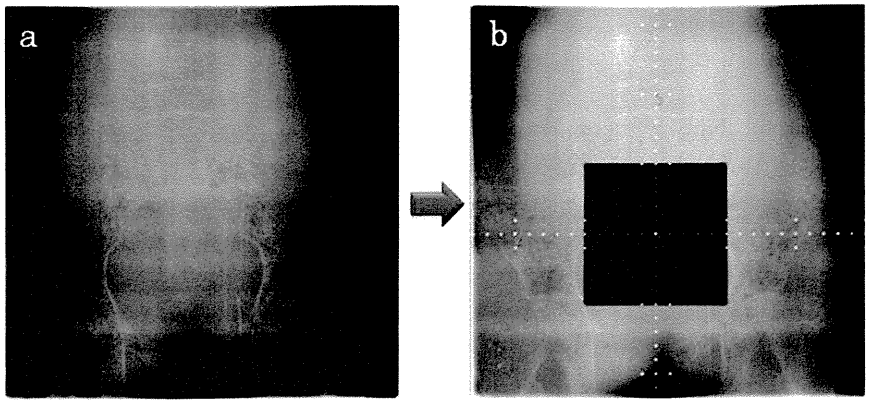


FIG.. 4. Portal image taken without field or scale tick marks (a). Automatically generated treatment field and scale ticks applied to the phantom portal image (b).

then asked to determine the same series of setup errors using the registration software, which we refer to as the "registration method". The automatic determination function of the software was also used to determine the setup error of the same case list ("automatic method"). Doctors and technicians were allowed to adjust image brightness and contrast. No time constraint was in place during the testing.

### E. Statistical analysis

The distance from actual and estimated offset was computed with $\sqrt{(x-x_0)^2+(y-y_0)^2}$ where (x, y) is the estimated offset and $(x_0, y_0)$ is the actual offset. The average and standard deviation of the distance was computed for each examiner.

The average consistency of an examiner was defined as the average geometric distance between two estimations of a single case. The mean of the methods was compared with the paired t-test. The difference of the average consistency among the three methods was also computed in order to determine if consistency improved using the software. All statistical analysis was performed with JMP version 8 (SAS Institute Inc., Cary, NC).

### F. Database study

In order to test the performance of the automatic registration mode of the software on actual clinical data, we assembled a database of over 5,000 patient setup cases performed between April 2007 and December 2009 at our hospital. At the time of treatment, the portal image for each case was registered with the corresponding DRR image using the manual mode of the software, and the setup error for each case was determined by a consensus of three people: a software operator (medical physicist), a radiation technician, and the attending oncologist. Although it is difficult to establish a "gold standard" for clinical data, for this study we assume the human-determined offset is correct, or at least very near the actual offset error.

After assembling the database, a large batch script was executed to open each case, fuse the portal and DRR images, and automatically determine the error offset using the MI optimization algorithm described above. The automatically-determined error offset was then compared with the human-determined error offset. The geometric distance between the two values was computed and a statistical analysis was performed.

## III. RESULTS

### A. Phantom study

The results of the thoracic and pelvis are shown in Fig. 5(a) and 5(b), respectively. The geometric distance from the actual offset and the determined offset is plotted. Results from five doctors (DR1–DR5) using the side-by-side method, four technicians (TECH1–TECH4) using the registration software in manual mode, and the automatic method (COMP) are shown.

For the thorax, the average distance between the actual setup error and the estimated error was 4.3 ± 3.0 mm for the radiation oncologists without the registration software, 2.1 ± 2.4 mm for technicians with the registration software, and 0.8 ± 0.4 mm for the automatic algorithm. For the pelvis, the average distance between the actual setup error and estimated error was 2.0 ± 0.5 mm for the radiation oncologists without the registration software, 2.5 ± 0.4 mm for technicians with the registration software, and 2.0 ± 1.0 mm for the automatic algorithm.

Each case was presented to the examiner twice. These two values are plotted vertically for each examiner. Consistency was measured as the geometric distance between the two estimated offsets of the same portal image. This corresponds to the height of the vertical bar in Fig. 5. The results are summarized in Table 1.

In order to determine statistically whether setup error estimation improved using the software, we computed the average consistency among the three methods. The average consistency for the side-by-side method was 2.4 ± 2.0 mm for thorax and 1.4 ± 1.2 mm for pelvis. The average

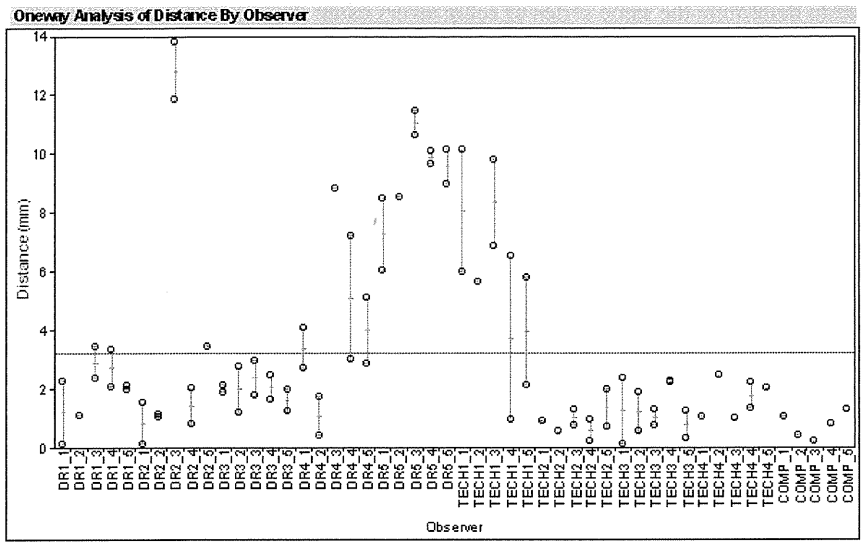


(a)

FIG. 5(a). Results of AP chest study.

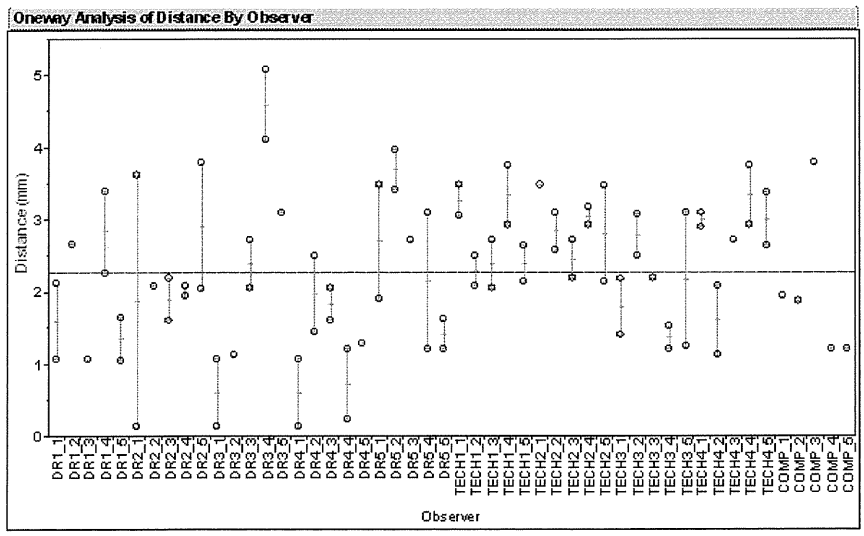


(b)

FIG. 5(b). Results of AP pelvis study.

consistency for the registration method was $1.7 \pm 1.6$ mm for thorax and $0.9 \pm 0.5$ mm for pelvis. The results are summarized in Table 2. Note that the computer algorithm always produces the same result for a given input, so it is perfectly consistent.

In order to test statistically that setup error estimation improved using the software, we computed the paired two samples for means. The null hypothesis is that population mean of the differences between the paired values is zero. The results are summarized in Tables 3(a) and 3(b).

TABLE 1. Average distance from estimated and actual setup error.

| *Phantom* | *Method* | *Average Distance* |
|---|---|---|
| Chest | Side-by-side | 4.3±3.0 mm |
| | Registration | 2.1±2.4 mm |
| | Auto | 0.8±0.4 mm |
| Pelvis | Side-by-side | 2.0±0.5 mm |
| | Registration | 2.5±0.4 mm |
| | Auto | 2.0±1.0 mm |

TABLE 2. Average consistency of test subjects.

| *Phantom* | *Method* | *Average Consistency* |
|---|---|---|
| Chest | Side-by-side | 2.4±2.0 mm |
| | Registration | 1.7±1.6 mm |
| Pelvis | Side-by-side | 1.4±1.2 mm |
| | Registration | 0.9±0.5 mm |

TABLE 3(a). Comparison of estimation methods (chest).

| *Comparison* | *p-value* |
|---|---|
| Side-by-side - Registration | 0.0067 |
| Side-by-side - Auto | 0.0002 |
| Registration - Auto | 0.0001 |

TABLE 3b. Comparison of estimation methods (pelvis).

| *Comparison* | *p-value* |
|---|---|
| Side-by-side - Registration | 0.0047 |
| Side-by-side - Auto | 0.4547 |
| Registration - Auto | 0.0593 |

## B. Database study

Results of the database study are summarized in Table 4. Overall, the automatic registration method does not perform well at around 7 mm from the human-estimated offset. However, for certain anatomical regions, such as head and breast, the algorithm consistently estimated the setup error within about 2 mm of the human estimation. Automatic registration was especially poor for pelvic regions — more than 1 cm on average. This is probably due to the lack of contrast in the portal images.

In order to demonstrate the usefulness of the automatic mode of operation for two sample anatomical cases, we arbitrarily divided the distance between the human and computer estimated offsets into four bins: ≤ 2 mm (Good), ≤ 5 mm (Fair), ≤ 10 mm (Poor) and > 10 mm (Terrible). Tables 5(a) and 5(b) show the results for head and pelvis cases for all gantry angles.

TABLE 4. Comparison of auto-shift function with clinical case database.

| *Group* | *Count* | *Mean Dist. (mm)* |
|---|---|---|
| All | 5101 | 7.0±2.1 |
| AP Head | 407 | 2.4±2.1 |
| LR Head | 537 | 2.2±2.7 |
| AP Neck | 158 | 5.5±6.1 |
| LR Neck | 214 | 4.2±4.3 |
| OB Neck | 95 | 4.8±4.1 |
| AP Chest | 264 | 5.1±4.5 |
| LR Chest | 101 | 7.7±8.0 |
| OB Breast | 160 | 3.6±2.7 |
| AP Pelvis | 148 | 13.8±19.8 |
| LR Pelvis | 148 | 12.8±11.7 |

TABLE 5(a). Comparison of auto-shift function with humans (head).

| *Bin* | *Frequency (total = 61)* |
|---|---|
| Good (≤2 mm) | 35 (57%) |
| Fair (≤5 mm) | 23 (38%) |
| Poor (≤10 mm) | 1 (2%) |
| Terrible (> 10 mm) | 2 (3%) |

TABLE 5(b). Comparison of auto-shift function with humans (pelvis).

| *Bin* | *Frequency (total = 48)* |
|---|---|
| Good (≤2 mm) | 4 (8%) |
| Fair (≤5 mm) | 9 (19%) |
| Poor (≤10 mm) | 16 (33%) |
| Terrible (> 10 mm) | 19 (40%) |

### C. Tilt experiment

Results of the tilt experiment are presented in Table 6. When the test point was placed 5 cm within the working area, the distance from the DRR point and the transformed portal image point was 0.7 mm. When the point was placed 5 cm outside the working area, the distance increased to 1.5 mm. This result indicates that the user must be careful to consider only bony structures within the working area when the out-of-plane tilt is large. The automatic registration algorithm should also ignore pixels outside the working area.

TABLE 6. Result of tilt experiment.

| *Point Placement* | *Distance* |
|---|---|
| Inside working area | 0.7 mm |
| Outside working area | 1.5 mm |

## IV. DISCUSSION

Our results show that the registration method was at least not worse than the side-by-side method, and the automatic method was statistically better than both the side-by-side method and registration method for the thorax phantom case studied. This result suggests that our

software can be a reasonable complementary method in the clinical practice. Based on this study, the software has been installed in our hospital information system and has been used in clinical practice since April 2007. Moreover, the time required for the estimation of the setup error has not been extended by the usage of this program, once the operator obtained sufficient experience with the software.

A number of criteria influenced our software design decisions:

- Because image registration is performed while the patient is waiting in the treatment position, the system must be fast — less than about one minute after the portal image is obtained.
- DRRs by any commercial planning software are to be used, as long as scale information is burned into the bitmap. The DRR image can even be a screen-captured bitmap, or a digital scan of a paper, or film print.
- Any common file format (e.g., bitmap, JPEG, DICOM) can be used for either the portal or DRR image.
- The system must work with any beam view of any anatomical region encountered in clinical practice.
- The software must run on a single standard PC running the Windows operating system.

We have found that there was a large inconsistency in the side-by-side method among doctors. This is probably due to a difference in training or experience. The large variation in the accuracy of the final decision based on the portal film may influence the clinical outcome. The improvement in the consistency with automatic registration (which was found in this study for thorax) may improve the local control rate and complication rate in this context.

If Dr. 5, in particular, is omitted, the side-by-side method compares well with the registration methods. Although Dr. 5 was a licensed radiation oncologist with experience estimating setup errors, he or she may have needed more practice with our experimental setup. Although we explained that the movement of the radiation field (rather than the treatment couch) should be specified, it is easy to mistake left-right or up-down shift. We feel that these kinds of human errors are inevitable when relying solely on human judgment with the side-by-side method.

From the database study, we can state that the automatic mode of operation performs well for head, neck and breast cases, but performs poorly for pelvic cases. Due to the thickness of the human anatomy in the pelvic and abdomen regions, the contrast of the resulting megavoltage portal image is very low. This makes automatic registration based on mutual information extremely difficult. In order to improve the performance of the automatic registration, the contrast of the portal image needs to be improved. Possible methods of improving portal image contrast include using kilovoltage X-ray, or using advanced digital image processing.[8] Other methods, such as restricting the area used to compute the mutual information may further improve auto-registration.

Although the automatic registration algorithm performed reasonably well on the pelvis phantom, the brightness and contrast (window level) of the portal image from the phantom image was adjusted by hand to maximize the contrast of the pelvic bone. In the database study, however, it was not feasible to adjust all cases by hand. The window level was computed automatically from the raw scanned data based on the histogram of pixel values. If the window level algorithm can be improved, the image contrast may be increased. Sophisticated image filters may also improve the signal-to-noise ratio and make bony features more recognizable. [9] We hope that this will, in turn, improve the auto-registration results.

While some verification systems are applicable to only a particular application (for example, lung cancer[10] or pelvic treatments[11]), our system is used for all cases encountered in our practice, including oblique views. Some systems require the computation of custom DRR images in order to match as closely as possible the portal image.[12] Our system uses the DRRs that are generated by a commercial TPS software package. Thus, the same pair of portal and DRR images that the attending physicians have normally been using are used by our software.

Some systems require the user to draw bony structures on the source images.[13] While this is an option with our software, it is not required. It is sometimes useful to draw the outline of a bone on both images, and then see how closely they align on the merged image; however, we found that this method significantly increases the burden on the operator. It is generally faster to view the merged portal-DRR image without hand-drawn contours.

Although EPID has become popular, some EPID systems are quite expensive to maintain and have reduced imaging quality. Our software can be used in many situations where good quality EPID is not available.

Because our system uses only three points to calculate the out-of-plane transformation, areas far from the control points (outside the working area) may not align exactly. If the entire image is to be used for alignment, an alternative method would be to use a calibration function such as McalList from the Matrox Imaging Library.[14] With this method, a list of corresponding points on the portal and DRR images is passed to the function and a perspective distortion correction matrix is calculated. The more points that are specified, the more accurate the mapping. However, because only points on the axes can be specified, the corners of the corrected portal image may still be slightly distorted. Specifying many points may also be a burden on the user. An automatic method of detecting all the visible grid tick marks on the portal and DRR images is under investigation.

## V. CONCLUSIONS

The ability to estimate offset values improved using our software for the chest phantom that we tested. Setup error estimation was further improved using our automatic error estimation algorithm. Estimations were not statistically different for the pelvis case. Comparing the automatic setup function with a database of clinical cases estimated by human operators revealed that the automatic function works relatively well for head, chest and breast cases, but performs poorly for pelvis and other cases. Automatic registration should improve by increasing the contrast of the portal image. Although setup error can be manually judged accurately and quickly with the software as an aid to doctors and technicians, work remains to make the software more fully automatic.

## REFERENCES

1. Hurkmans CW, Remeijer P, Lebesque JV, Mijnheer BJ. Set-up verification using portal imaging: review of current clinical practice. Radiother Oncol. 2001;58(2):105–20.
2. Clippe S, Sarrut D, Malet C, Miquet S, Ginestet C, Carrie C. Patient setup error measurement using 3D intensity-based image registration techniques. Int J Radiat Oncol Biol Phys. 2003;56(1):259–65.
3. Boyer AL. Antonuk L, Fenster A, et al. A review of electronic portal imaging devices (EPIDs). Med Phys. 1992;19(1):1–16.
4. Shirato H, Shimizu S, Kunieda T, et al. Physical aspects of a real-time tumor-tracking system for gated radiotherapy. Int J Radiat Oncol Biol Phys. 2000;48(4):1187–95.
5. Sorcini B and Tilikidis A. Clinical application of image-guided radiotherapy, IGRT (on the Varian OBI platform). Cancer/Radiothér. 2006;10(5):252–57.
6. Pluim J, Maintz J, Viergever M. Mutual-information-based registration of medical images: a survey. IEEE Trans Med Imaging. 2003;22(8):986–1004.
7. Tsao J. Interpolation artifacts in multimodality image registration based on maximization of mutual information. IEEE Trans Med Imaging. 2003;22(7):854–64.
8. Nakashima K, Ashizawa K, Ochi M, et al. Interpretation of normal anatomical structures on chest radiography: comparison of Fuji computed radiography (FCR) 5501D with FCR 5000 and screen-film system. J Appl Clin Med Phys. 2003;4(1):85–90.
9. Yamada S, and Murase K. Effectiveness of flexible noise control image processing for digital portal images using computed radiography. Br J Radiol. 2005;78(930):519–27.
10. Van Sörensen de Koste JR, De Boer HCJ, Schuchhard-Schipper RH, Senan S, Hejimen BJ. Procedures for high precision setup verification and correction of lung cancer patients using CT-simulation and digitally reconstructed radiographs (DRR). Int J Radiat Oncol Biol Phys. 2003;55(3):804–10.

11. Hanley J, Mageras GS, Sun J, Kutcher GJ. The effects of out-of-plane rotations on two dimensional portal image registration in conformal radiotherapy of the prostate. Int J Radiat Oncol Biol Phys. 1995;33(5):1331–43.
12. Dong L, and Boyer A. An image correlation procedure for digitally reconstructed radiographs and electronic portal images. Int J Radiat Oncol Biol Phys. 1995;33(5):1053–60.
13. Lujan AE, Balter JM, Ten Haken RK. Determination of rotations in three dimensions using two-dimensional portal image registration. Med Phys. 1998;25(5):703–08.
14. Matrox Electronic Systems. Matrox imaging library, version 9: user guide. Manual no. Y10513-301-0900. Dorval (HQ), Canada: Matrox Electronic Systems Ltd.; 2008. p. 200–01.

Optimization of fluoroscopy parameters using pattern matching prediction in the real-time tumor-tracking radiotherapy system



2011 Phys. Med. Biol. 56 4803

(http://iopscience.iop.org/0031-9155/56/15/011)

IOP PUBLISHING PHYSICS IN MEDICINE AND BIOLOGY

Phys. Med. Biol. **56** (2011) 4803–4813 doi:10.1088/0031-9155/56/15/011

# Optimization of fluoroscopy parameters using pattern matching prediction in the real-time tumor-tracking radiotherapy system

**Naoki Miyamoto[1], Masayori Ishikawa[1], Gerard Bengua[2], Kenneth Sutherland[1], Ryusuke Suzuki[2], Suguru Kimura[3], Shinichi Shimizu[3], Rikiya Onimaru[3] and Hiroki Shirato[3]**

[1] Division of Medical Physics and Engineering, Graduate School of Medicine, Hokkaido University, Sapporo, Japan
[2] Department of Medical Physics, Hokkaido University Hospital, Sapporo, Japan
[3] Department of Radiology, Graduate School of Medicine, Hokkaido University, Sapporo, Japan

E-mail: miya-nao@med.hokudai.ac.jp

Received 13 March 2011, in final form 15 June 2011
Published 13 July 2011
Online at stacks.iop.org/PMB/56/4803

**Abstract**

In the real-time tumor-tracking radiotherapy system, fluoroscopy is used to determine the real-time position of internal fiducial markers. The pattern recognition score (PRS) ranging from 0 to 100 is computed by a template pattern matching technique in order to determine the marker position on the fluoroscopic image. The PRS depends on the quality of the fluoroscopic image. However, the fluoroscopy parameters such as tube voltage, current and exposure duration are selected manually and empirically in the clinical situation. This may result in an unnecessary imaging dose from the fluoroscopy or loss of the marker because of too much or insufficient x-ray exposure. In this study, a novel optimization method is proposed in order to minimize the fluoroscopic dose while keeping the image quality usable for marker tracking. The PRS can be predicted in a region where the marker appears to move in the fluoroscopic image by the proposed method. The predicted PRS can be utilized to judge whether the marker can be tracked with accuracy. In this paper, experiments were performed to show the feasibility of the PRS prediction method under various conditions. The predicted PRS showed good agreement with the measured PRS. The root mean square error between the predicted PRS and the measured PRS was within 1.44. An experiment using a motion controller and an anthropomorphic chest phantom was also performed in order to imitate

  

a clinical fluoroscopy situation. The result shows that the proposed prediction method is expected to be applicable in a real clinical situation.

(Some figures in this article are in colour only in the electronic version)

## 1. Introduction

The real-time tumor-tracking radiotherapy (RTRT) system was developed (Shirato *et al* 1999) in order to compensate for respiratory-induced motion of tumors. The system consists of a linear accelerator (linac) and two x-ray fluoroscopy systems. In the RTRT system, metal markers are surgically embedded in or near the target tumor. During radiation treatment, the markers are detected by means of continuous fluoroscopy operated at 30 frames $s^{-1}$. The linac irradiation is only enabled during the period when the detected location of the fiducial marker is within its allowed displacement values with respect to the treatment plan. The location of the inserted fiducial marker is calculated from the projected position in the pair of the fluoroscopic images obtained at two different directions. The marker position on each fluoroscopic image is determined by means of a template pattern matching technique which is based on the normalized cross correlation between the template image and the target image. The pattern recognition score (PRS) is defined by the correlation coefficient. The location that gives the highest PRS is considered to be the marker position in the search area. With high tube voltage, large current and long exposure, the PRS will be higher because a high-signal-to-noise-ratio (SNR) fluoroscopic image can be obtained. In this case, the marker can be tracked accurately and stably; however, the radiation dose due to x-ray fluoroscopy also increases. With many treatment fractions or in long treatment duration of a single fraction, the total imaging dose could be more than what clinically acceptable. On the other hand, by decreasing the fluoroscopy parameter settings, the PRS is decreased and the fiducial marker could be lost. During irradiation, the fluoroscopy parameters such as tube voltage, current and exposure duration are selected manually and empirically. This may result in unnecessary imaging dose from the fluoroscopy or loss of the marker because of too much or insufficient x-ray exposure. Hence, the fluoroscopy parameters have to be adjusted taking into account both the PRS and the fluoroscopic dose.

Optimization of the operating parameters has been investigated and examined in computer tomography (Brisse *et al* 2007, Papadakis *et al* 2008), radiation diagnostic (Doyle *et al* 2005, Ullman *et al* 2006) or mammography (Williams *et al* 2008, Young *et al* 2006). In these radiation diagnostic devices, the optimum tube voltage, current or exposure duration are optimized in consideration of the contrast-to-noise ratio (CNR) or the SNR of the x-ray image. However, the optimization method based on these indices cannot be applied in the RTRT system because the marker moves in various regions of the fluoroscopic image due to respiration. Therefore, it is difficult to determine the relationship between the PRS and the indices of image quality such as CNR or SNR.

In order to minimize the fluoroscopic dose by reducing the pulse rate of the fluoroscopy, various prediction models of tumor movement have been reported (Ruan *et al* 2007, Sharp *et al* 2004). A combination with external signals such as a real-time position management system is also useful for dose reduction (Wu *et al* 2008). Placing an additional filtration material in the fluoroscopic beam (Moore *et al* 2008, Young *et al* 2006) should be useful for the RTRT system. Optimization of the fluoroscopy parameters is one of the best solutions for dose reduction. However, this has not been established yet for the RTRT system.

In the RTRT system, optimization should be focused on reduction of the radiation dose while maintaining the PRS at an acceptable level. For this purpose, we propose a novel optimization method based on prediction of the PRS at an arbitrary position in the fluoroscopic image. In the proposed method, the PRS can be predicted in a region where the marker appears to move in the fluoroscopic image. The predicted PRS can be utilized to judge whether the marker can be tracked with accuracy and stability. Hence, by analyzing the fluoroscopic images obtained in several x-ray tube settings, the best fluoroscopic setting can be derived. This method could be applied not only to the RTRT system but also to other fluoroscopy-based motion tracking systems that use the template pattern matching technique. The purpose of this research is to show the feasibility of the PRS prediction method and to demonstrate the optimization of the fluoroscopy parameters in a phantom study.

## 2. Materials and methods

### *2.1. Template pattern matching*

In the RTRT system, the fiducial marker is tracked every 0.033 s. On each sequential image, the marker position in the fluoroscopic image is recognized by means of a template pattern matching technique. The template image of the fiducial marker has to be registered in advance. In the RTRT system, the fluoroscopic image of the fiducial marker which is captured before insertion into the patients is used as the template image. In general, the same template image is applied to all treatments because the markers are manufactured with same specification. Template pattern matching is based on normalized cross correlation. The correlation coefficient is given by

$$r = \frac{N\sum_{i=1}^{N} I_i M_i - \left(\sum_{i=1}^{N} I_i\right)\sum_{i=1}^{N} M_i}{\sqrt{\left|N\sum_{i=1}^{N} I_i^2 - \left(\sum_{i=1}^{N} I_i\right)^2\right|\left|N\sum_{i=1}^{N} M_i^2 - \left(\sum_{i=1}^{N} M_i\right)^2\right|}}, \tag{1}$$

where $N$ is the pixel number, and $I_i$ and $M_i$ are the pixel values of the target image and the template image, respectively. The target image has to be cropped from the fluoroscopic image with the same size of the template image. The PRS is defined as

$$\mathrm{PRS} = \begin{cases} 0 & (r < 0), \\ 100 \times r^2 & (r \geqslant 0). \end{cases} \tag{2}$$

In our case, we are not interested in the negative value, so results are clipped to 0. The location that gives the highest PRS is considered to be the marker position in the search area. Other algorithms for determining the marker position have also been considered; however, they are not discussed in this paper.

In order to avoid the misidentification of the marker and to track only the marker, the threshold value of the PRS should be determined beforehand. If the maximum PRS in the search area is greater than the threshold value, the location that gives the highest PRS is considered to be the marker position. On the other hand, in case the maximum PRS is lower than the threshold value, the system decides that no markers are within the search area. If a high threshold value is applied, tracking accuracy is improved; however, the probability of losing the track of the marker is also increased. If a low threshold is used, the probability of the marker misidentification is increased. Hence, we must adjust the threshold value taking into account both tracking accuracy and stability.

The PRS depends on the quality of the fluoroscopic images. Assuming that a stable marker is tracked with the same exposure condition, the PRS fluctuates on each sequential image in fluoroscopy. This is mainly caused by the statistical noise of a digital x-ray image

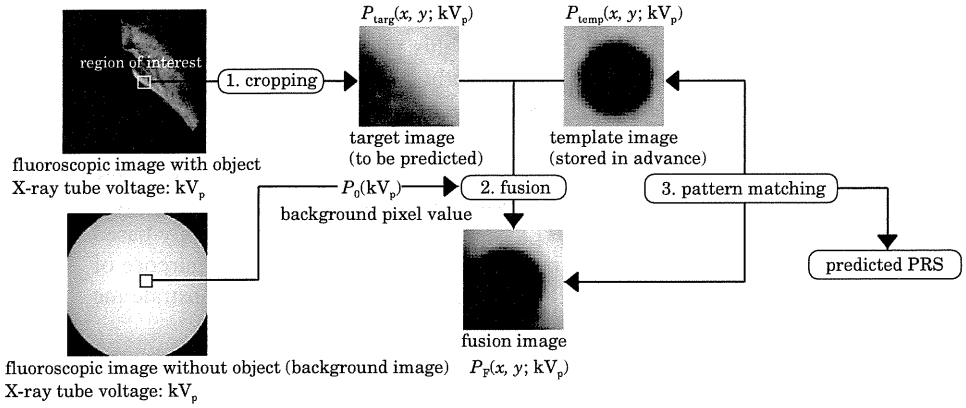


**Figure 1.** Outline of the pattern recognition score (PRS) prediction method.

(e.g. quantum noise, electronic noise). In a higher SNR image, the fluctuation of the PRS is smaller. Fluctuation of the PRS is correlated with that of the projected marker position in the fluoroscopic images. The 3D marker coordinates calculated by the RTRT system are also altered according to these fluctuations. The fluctuation of the 3D coordinates can be regarded as the tracking accuracy. As a result, the PRS can be one of the indicators of tracking accuracy. The relationship between the PRS and the tracking accuracy will depend on the characteristics of the imaging devices of the fluoroscopy system. Therefore, the relationship should be investigated in order to assure tracking accuracy for each system.

### 2.2. *PRS prediction algorithm*

The outline of the PRS prediction method is shown in figure 1. For simplicity, the parameter for optimization is assumed to be the x-ray tube voltage, $kV_p$. Other parameters, tube current and exposure duration, can be optimized in the same manner. The proposed prediction algorithm is a three-step procedure. First, the target area for PRS prediction is cropped from the fluoroscopic image with the same size as that of the template image. The pixel value distribution of the template image and the cropped target area obtained in a specific x-ray tube voltage $kV_p$ are defined as $P_{temp}(x, y; kV_p)$ and $P_{targ}(x, y; kV_p)$, respectively. An x-ray attenuation factor for each pixel position is calculated by taking into account the pixel value of the background image which is obtained without the objects. The background images should be obtained for each exposure setting in advance. The attenuation factor distributions of the template image and the target image are defined as

$$A_{temp}(x, y; kV_p) = -\ln \frac{P_{temp}(x, y; kV_p)}{P_0(kV_p)}, \tag{3}$$

$$A_{targ}(x, y; kV_p) = -\ln \frac{P_{targ}(x, y; kV_p)}{P_0(kV_p)}, \tag{4}$$

where $P_0(kV_p)$ is defined as the average pixel value of the background image. In order to consider the ununiformity of the background image, the location of the background image is selected according to the position where the template image is placed. Second, a fused image

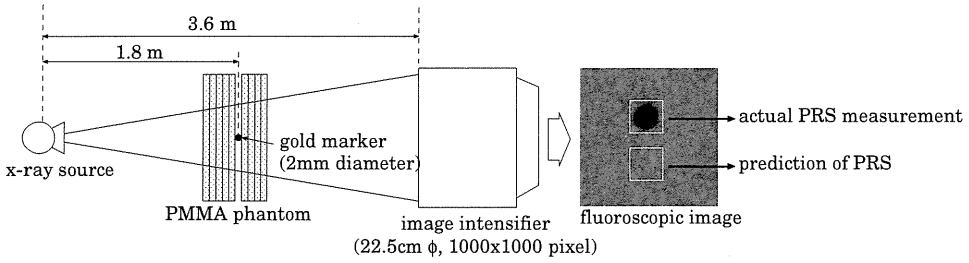


**Figure 2.** Experimental setup for examination of the relationship between the PRS and the tracking accuracy. This same setup was used for verification of the PRS prediction algorithm.

is constructed by assuming that the marker is within the cropped area. By considering the x-ray attenuation factor, the predicted pixel value distribution can be expressed as

$$P_F(x, y; \mathrm{kV_p}) = P_0(\mathrm{kV_p}) \exp\{-A_{\mathrm{temp}}(x, y; \mathrm{kV_p}) - A_{\mathrm{targ}}(x, y; \mathrm{kV_p})\}, \quad (5)$$

where the $P_F(x, y; \mathrm{kV_p})$ is the pixel value distribution of the predicted fusion image. Finally, the predicted PRS value is calculated by performing template pattern matching between the fused image $P_F(x, y; \mathrm{kV_p})$ and the template image $P_{\mathrm{temp}}(x, y; \mathrm{kV_p})$. In principle, the beam-hardening effect should be considered in order to construct the actual fusion image. The x-ray units used in this study have a filtration material which can remove the low-energy x-ray. Hence, the beam-hardening effect is no longer considered in this study. The effect of beam-hardening is to be addressed in future work.

The PRS at an arbitrary position in the fluoroscopic image can be predicted by the above procedures. By predicting the PRS in a region where the fiducial marker is expected to move in the fluoroscopic image, the tracking accuracy and stability can be evaluated without additional fluoroscopic dose. By processing the images obtained in different fluoroscopy settings, the optimum condition that gives the minimum fluoroscopic dose while maintaining the tracking accuracy at an acceptable level can be determined.

### *2.3. Experiments*

*2.3.1. Relationship between the tracking accuracy and the PRS.* First, the relationship between the PRS and the fluctuation of the measured 3D coordinates of the fiducial marker was investigated. The experimental setup is illustrated in figure 2. The distance between the x-ray source and the x-ray image intensifier (I.I.) was fixed at 3.6 m. The I.I. had an input of 22.5 cm diameter and was coupled to a 1000 × 1000 pixel resolution CCD camera. A 2.0 mm ∅ gold fiducial marker was placed at the isocenter and was sandwiched by polymethylmethacrylate (PMMA) slabs which have an area of 300 mm × 400 mm. In order to vary the PRS, the total thickness of the PMMA phantom was varied between 40 and 200 mm. Under each exposure condition, both the PRS and the recognition position on the fluoroscopic image were recorded 100 times every 0.033 s. The standard deviation (SD) of the recorded 100 recognition positions was converted to the SD of the 3D marker coordinates. The SD of the 3D marker coordinates should correspond to the tracking accuracy. Hence, the relationship between the PRS and the tracking accuracy was derived from this experiment.

*2.3.2. Verification of the PRS prediction.* Verification of the PRS prediction was performed with the same geometry as shown in figure 2. The tube current and tube exposure time were

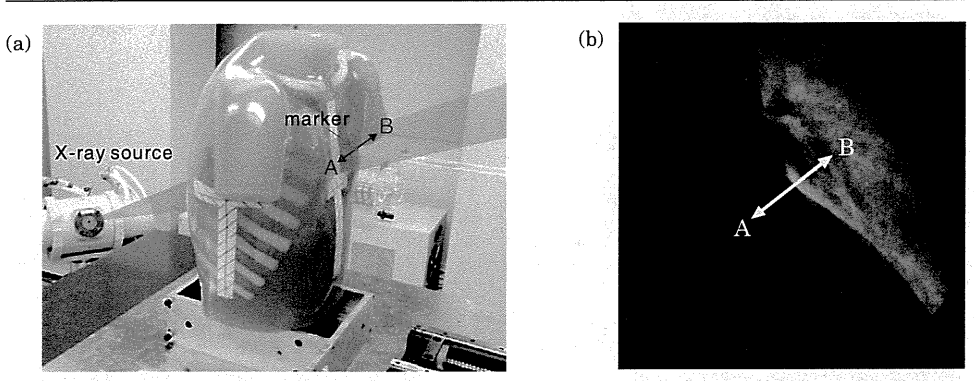


**Figure 3.** (a) Experimental setup for the phantom study. (b) An example of the x-ray fluoroscopic image. The marker was moved linearly between A and B.

fixed to 80 mA and 3 ms, respectively. By assuming that the image quality around the marker should be the same, the PRS was predicted from the area near the actual marker position as shown in figure 2. The template images and the background images, which corresponded to $P_{\text{temp}}(x, y; \text{kV}_\text{p})$ and $P_0(\text{kV}_\text{p})$, respectively, were recorded in each experimental x-ray tube voltage in advance. The experiment involved two scenarios. The first case was a variable x-ray tube voltage ranging from 40 to 90 $\text{kV}_\text{p}$ with 2 $\text{kV}_\text{p}$ increment, and fixed PMMA thickness of 80 mm. The PMMA thickness of 80 mm was assumed to be equal to an imaging condition of lung fluoroscopy. The second case was a fixed tube voltage of 50 $\text{kV}_\text{p}$ and the variable PMMA thickness ranging from 0 to 180 mm. The increment of the thickness was 20 mm. The PMMA thickness of 180 mm was assumed to be equal to a typical patient thickness (Vano *et al* 2006). The PMMA thickness was varied in order to imitate the marker overlapped in the variable density including the lung, bone and so on. It was confirmed in advance that the minimum tube voltage to recognize the marker was around 50 $\text{kV}_\text{p}$ in this PMMA thickness range. In order to consider the fluctuation of the measured PRS and the predicted PRS, the fluoroscopic image was acquired ten times on each exposure setup. The measured and the predicted PRS were compared to assess the prediction accuracy.

*2.3.3. Phantom study.* In order to confirm the accuracy of the PRS prediction in a clinical fluoroscopy situation, an experiment using a motion controller and an anthropomorphic chest phantom was performed. The experimental setup is shown in figure 3(a). Alignment of the x-ray tube and the I.I. was the same as in the previous experiments. The marker was placed in front of the phantom and was moved using the motion controller to mimic respiratory marker motion. The marker was moved linearly in the left–right direction of the phantom with a speed of 10 $\text{mm sec}^{-1}$. In the obtained fluoroscopic images, the marker moved within a region of varying media which included the lung, bone and heart. An example of the fluoroscopic image is shown in figure 3(b). The white arrow indicates the marker trajectory in the fluoroscopic image. The motion of the marker was tracked using the RTRT system, and both the PRS and the recognized position were recorded every 0.033 s. The x-ray tube voltage was varied from 46 to 54 $\text{kV}_\text{p}$ with 2 $\text{kV}_\text{p}$ increments. The tube current and exposure time were fixed to 80 mA and 3 ms, respectively. After gathering the sets of PRS and recognized positions along the marker trajectory, an image was captured without the marker. The fluoroscopic image

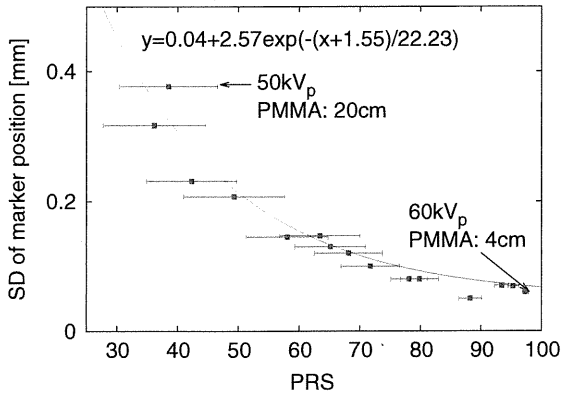


**Figure 4.** Relationship between the PRS and the SD of the 3D marker location. The solid line is a fitting curve.

without the marker was used for PRS prediction. The measured PRS and the predicted PRS were compared for each tube voltage.

## 3. Results

### *3.1. Relationship between the tracking accuracy and the PRS*

The relationship between the PRS and the SD of the 3D marker coordinates is shown in figure 4. The horizontal error bars represent the SD of the PRS in 100 times measurements under the same exposure condition. That was mainly caused by the statistical noise of the fluoroscopic image. In the case of large thickness of PMMA or low tube voltage, the PRS was decreased because of the low SNR of the image. In addition, the SD of the PRS was increased for the same reason. The marker was not able to be recognized correctly in the PRS region below 30. In contrast, the PRS was increased with thinner PMMA or high tube voltage. The PRS never reached 100 because an image that is exactly same as the template image is not able to be observed in the fluoroscopic image due to statistical noise of the image.

Curve fitting was applied in order to define the relationship between the PRS and the SD of the 3D coordinates. The SD is regarded as the tracking accuracy. In our experiment, it was found that the tracking accuracy could be kept within about 0.1 mm when the PRS exceeds about 75 during the marker tracking. It was almost equal to imaging resolution. Hence, the threshold PRS of 75 was considered to be suitable for accurate marker tracking in our experimental setup.

### *3.2. Verification of the prediction method*

The result of variable x-ray tube voltage with fixed PMMA thickness of 80 mm is shown in figure 5(a). Each point represents 2 $kV_p$ increments. The predicted PRS showed good agreement with the measured PRS. The SD of both the prediction and the measurement in the high PRS region was found to be smaller than that of the low-PRS region. The SD depended on the image quality as mentioned above. By taking account of the 2kV increment, it was found that the PRS decreased drastically at a typical x-ray tube voltage. Hence, it would be difficult to determine the optimum tube voltage by manual operation. In order to evaluate the

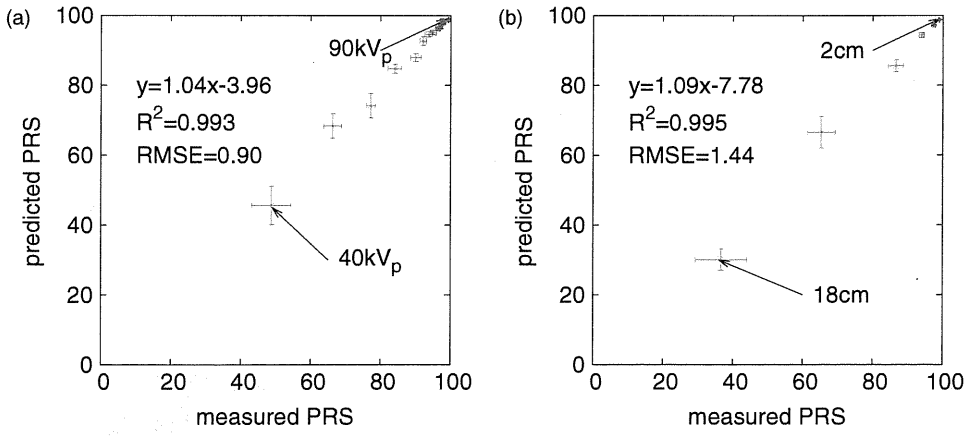


**Figure 5.** Measured and predicted PRS: (a) constant thickness and variable tube voltage and (b) constant tube voltage and variable thickness.

prediction accuracy, the coefficient of determination $R^2$ was derived from linear regression between the predicted PRS and the measured PRS. The root mean square error (RMSE) was also calculated as a prediction error. In the case of variable x-ray tube voltage and fixed PMMA thickness, $R^2 = 0.993$ and RMSE $= 0.90$ were obtained. The relationship between the predicted PRS and the measured PRS showed good linearity. In addition, the RMSE was within the statistical error. Hence, the PRS could be predicted within acceptable discrepancy in the case of variable x-ray tube voltage.

The result of variable PMMA thickness with fixed tube voltage of 50 $kv_p$ is shown in figure 5(b). The SD of both the measured PRS and the prediced PRS was increased as PMMA thickness was increased. In this case, $R^2 = 0.995$ and RMSE $= 1.44$ were obtained. The RMSE was larger compared with the result of fixed PMMA thickness. One of the reasons was assumed to be the beam-hardening effect. However, the prediction error could be mainly caused by the statistical noise as mentioned above. Hence, the discrepancy between the measured PRS and the predicted PRS could be permissible. It was confirmed that the proposed method can predict the PRS in both cases of varying tube voltage and varying object thickness. The patient's couch will be overlapped in the fluoroscopic images in the actual clinical case. The effect of the x-ray absorbance by the couch is to be addressed in future work.

### *3.3. Phantom study*

The results of the measured PRS and the predicted PRS along the marker trajectory for each x-ray tube voltage are shown in figure 6. The measured PRS and the predicted PRS showed the same trend for each tube voltage. The RMSE was decreased as the tube voltage was increased. This was mainly caused by the improvement of the SNR. As shown in figure 3(b), region A was a thick region which included the heart and bone. Region B was less dense compared to region A, including only the lung region. The SNR of the fluoroscopic image captured in region A should be lower than that of region B. Hence, the PRS of region A was relatively low compared to that of region B.

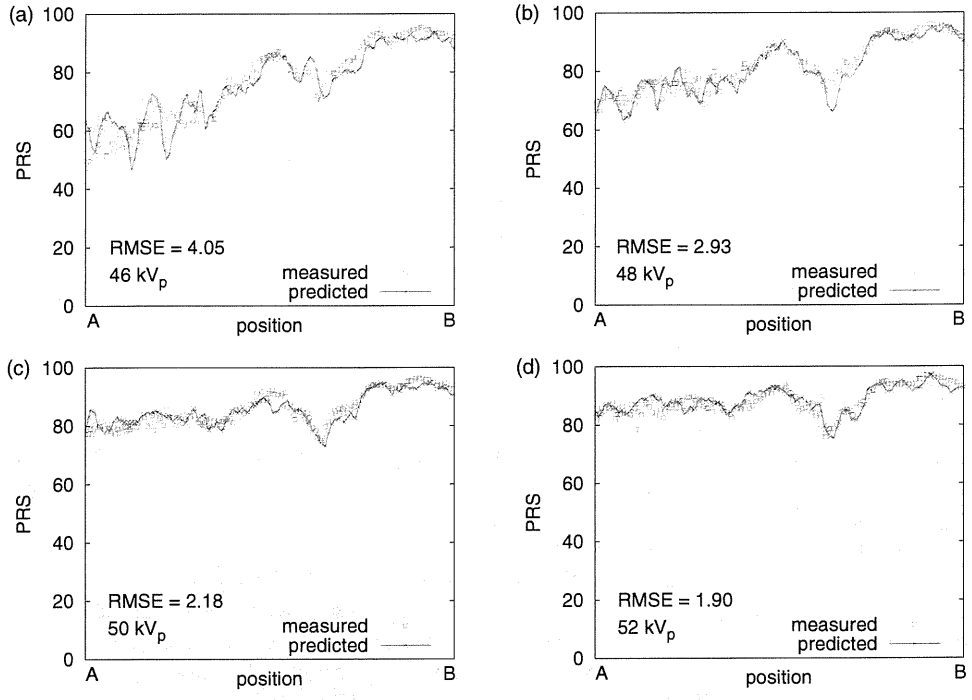


**Figure 6.** Measured and predicted PRS for each x-ray tube voltage: (a) 46 $kV_p$, (b) 48 $kV_p$, (c) 50 $kV_p$ and (d) 52 $kV_p$.

The PRS at the boundary between region A and region B could not be improved even if the tube voltage was increased. One reason was that the brightness of the target image in the border area was clearly separated. In our experiments, the predicted PRS showed the same trend as the measured PRS along the marker trajectory including the border region. In the clinical situation, the fluoroscopic images contain a large variation of the pixel value distribution. Hence, the proposed prediction method is expected to be applicable in a real clinical situation.

## 4. Discussion

The optimization procedure based on PRS prediction is discussed by taking an example from the results of the phantom study. For the purpose of optimization, the pass-rate is defined as a ratio of the number of the points that exceed the threshold PRS and the number of all points. The threshold PRS of 75, which corresponds to about 0.1 mm tracking accuracy, was applied in the analysis. The RMSE and pass-rate are summarized in table 1. The predicted pass-rate showed good agreement with the measured pass-rate. The difference between the measured and the predicted pass-rate was within 2.3% in our experiments. The tube parameters are optimized when the pass-rate is almost 100%. The optimum tube voltage was estimated to be either 50 $kV_p$ or 52 $kV_p$ in our fluoroscopic setup. Tube parameters, such as current and exposure time, can also be optimized in the same manner. Thus, the best fluoroscopic condition can be derived by analyzing the images captured in different tube settings.

**Table 1.** RMSE and the pass-rate for each tube voltage.

| | | Pass-rate (%) | |
|---|---|---|---|
| Tube voltage ($kV_p$) | RMSE of PRS | Measured | Predicted |
| 46 | 4.05 | 50.7 | 48.4 |
| 48 | 2.93 | 71.6 | 73.1 |
| 50 | 2.18 | 98.4 | 97.1 |
| 52 | 1.90 | 100.0 | 99.7 |
| 54 | 1.83 | 100.0 | 100.0 |

It has been reported that the skin surface dose rate from RTRT could be as high as 1 Gy $h^{-1}$ (Shirato *et al* 2000b). The exposure time of the fluoroscopy could extend for more than 30 min in a specific case such as irregular motion of the tumor. Assuming the worst case, the cumulative dose due to the fluoroscopy could reach an unacceptable value of 1Gy, which is referenced as a limit level in interventional radiology (Vano *et al* 2009). Hence, the optimization of the fluoroscopic parameters is strongly required for dose reduction. For example, a nominal x-ray tube voltage from 90 $kV_p$ to 110 $kV_p$, tube current of 100 mA and pulse width of 4 ms are used in the actual RTRT irradiation of the lung region. The experimental setup for this study was based on actual lung treatments. It was shown that the tube voltage can be reduced to the minimum value while maintaining the PRS at an acceptance level. For example, if the tube voltage can be reduced from 90 $kV_p$ to 50 $kV_p$, the fluoroscopic dose can be reduced by about 80%. Hence, the imaging dose could be reduced significantly by the proposed method.

By reducing the tube voltage manually at small increments while tracking the marker, the optimum tube voltage may be defined. In manual operation, however, the marker should be tracked for a long time, which includes many respiratory cycles, in order to confirm the tracking stability. This is because the marker does not always move on the same trajectory. Hence, more time and additional dose are needed for manual optimization. In contrast, our proposed method can predict the PRS at an arbitrary position where the marker is expected to move. The optimized fluoroscopy condition can be determined quickly by considering whether or not the predicted pass-rate is acceptable. In actual treatment, respiration affects both the motion of the marker and the adjacent organs. Hence, the PRS should be predicted in the region of the marker trajectory including an additional margin.

If the digitally reconstructed radiographs (DRRs), which are reconstructed by a planning computer tomography (CT), can be used as the fluoroscopic images, the pseudo-target could be created by adding the template images and the background images to the DRRs without the actual fluoroscopic images. However, problems such as the resolution of the CT images, the inconsistency of the imaging condition between the CT and the fluoroscopy and so on should be solved.

## 5. Conclusion

A technique for the optimization of x-ray fluoroscopy in the RTRT system was investigated. It was confirmed that the proposed method can predict the PRS in both cases of varying tube voltage and varying object thickness. In addition, the optimum fluoroscopy parameter was derived while keeping the PRS high enough to track the marker accurately. As a result, the proposed optimization method based on PRS prediction can be applicable in the RTRT system.

This method could also be used for other systems that use the motion tracking technique based on template pattern matching.

## Acknowledgments

A part of this research is granted by the Japan Society for the Promotion of Science (JSPS) through the 'Funding Program for World-Leading Innovative R&D on Science and Technology (FIRST Program)' initiated by the Council for Science and Technology Policy (CSTP). A part of this work belongs to 'Research and Development Project on Treatment Equipment Using High Accurate X-Ray Radiation' which Hokkaido University contracted with New Energy and Industrial Technology Development Organization (NEDO).

## References

Brisse H J, Madec L, Gaboriaud G, Lemoine T, Savignoni A, Neuenschwander S, Aubert B and Rosenwald J C 2007 Automatic exposure control in multichannel CT with tube current modulation to achieve a constant level of image noise: experimental assessment on pediatric phantoms *Med. Phys.* 34 3018–33

Doyle P, Martin C J and Gentle D 2005 Dose-image quality optimisation in digital chest radiography *Radiat. Prot. Dosim.* 114 269–72

Moore C S, Beavis A W and Saunderson J R 2008 Investigation of optimum x-ray beam tube voltage and filtration for chest radiography with a computed radiography system *Br. J. Radiol.* 81 771–7

Papadakis A E, Perisinakis K and Damilakis J 2008 Automatic exposure control in pediatric and adult multidetector CT examinations: a phantom study on dose reduction and image quality *Med. Phys.* 35 4567–76

Ruan D, Fessler J A and Balter J M 2007 Real-time prediction of respiratory motion based on local regression methods *Phys. Med. Biol.* 52 7137–52

Sharp G C, Jiang S B, Shimizu S and Shirato H 2004 Prediction of respiratory tumour motion for real-time image-guided radiotherapy *Phys. Med. Biol.* 49 425–40

Shirato H *et al* 2000b Physical aspects of a real-time tumor-tracking system for gated radiotherapy *Int. J. Radiat. Oncol. Biol. Phys.* 48 1187–95

Shirato H, Shimizu S, Shimizu T, Nishioka T and Miyasaka K 1999 Real-time tumor-tracking radiotherapy *Lancet* 353 1331–2

Ullman G, Sandborg M, Dance D R, Hunt R A and Alm Carlsson G 2006 Towards optimization in digital chest radiography using Monte Carlo modelling *Phys. Med. Biol.* 51 2729–43

Vano E *et al* 2009 Patient dose reference levels for interventional radiology: a national approach *Cardiovasc. Intervent. Radiol.* 32 19–24

Vano E, Gonzalez L, Fernandez J M, Prieto C and Guibelalde E 2006 Influence of patient thickness and operation modes on occupational and patient radiation doses in interventional radiology *Radiat. Prot. Dosim.* 118 325–30

Williams M B *et al* 2008 Optimization of exposure parameters in full field digital mammography *Med. Phys.* 35 2414–23

Wu H, Zhao Q, Berbeco R I, Nishioka S, Shirato H and Jiang S B 2008 Gating based on internal/external signals with dynamic correlation updates *Phys. Med. Biol.* 53 7137–50

Young K C, Oduko J M, Bosmans H, Nijs K and Martinez L 2006 Optimal beam quality selection in digital mammography *Br. J. Radiol.* 79 981–90